

CELL BIOLOGY

A reconstituted mammalian APC-kinesin complex selectively transports defined packages of axonal mRNAs

Sebastian Baumann¹, Artem Komissarov¹, Maria Gili¹, Verena Ruprecht¹, Stefan Wieser³, Sebastian P. Maurer^{1,2*}

Through the asymmetric distribution of messenger RNAs (mRNAs), cells spatially regulate gene expression to create cytoplasmic domains with specialized functions. In neurons, mRNA localization is required for essential processes such as cell polarization, migration, and synaptic plasticity underlying long-term memory formation. The essential components driving cytoplasmic mRNA transport in neurons and mammalian cells are not known. We report the first reconstitution of a mammalian mRNA transport system revealing that the tumor suppressor adenomatous polyposis coli (APC) forms stable complexes with the axonally localized β -actin and β 2B-tubulin mRNAs, which are linked to a kinesin-2 via the cargo adaptor KAP3. APC activates kinesin-2, and both proteins are sufficient to drive specific transport of defined mRNA packages. Guanine-rich sequences located in 3'UTRs of axonal mRNAs increase transport efficiency and balance the access of different mRNAs to the transport system. Our findings reveal a minimal set of proteins sufficient to transport mammalian mRNAs.

INTRODUCTION

By localizing mRNAs and producing proteins locally, cells spatially control gene expression, allowing them to build local protein networks with specialized functions (1–3). Different cell types localize up to thousands of different mRNAs to specific domains, which is required for a wide range of cellular functions (4–9). Multiple approaches shed light on the importance, complexity, and mechanisms of mRNA localization: New imaging techniques allowed to visualize individual mRNA transport events in living neurons (10, 11), insightful proteomic approaches provided a rich repertoire of candidates potentially involved in mammalian mRNA transport (12, 13), and in vitro reconstitutions revealed the first sets of essential components of yeast and *Drosophila* mRNA transport systems (14–17). However, as crucial building blocks of these reconstituted transport systems lack mammalian homologs and proteomics studies could not identify the essential components linking mRNAs to motor proteins, it remained unknown how any mammalian mRNA is loaded onto motor proteins, how copy number of transported mRNAs is controlled, and what molecular mechanisms generate specificity to transport only certain mRNAs. If the minimal components of a mammalian mRNA transport system can be identified and purified, an in vitro reconstitution would provide the means to address these fundamental questions.

Adenomatous polyposis coli (APC) binds the KAP3 cargo-loading subunit of the heterotrimeric kinesin-2 KIF3A/B/KAP3 (18), microtubules (19, 20), and guanine-rich RNA sequences present in the 3' untranslated regions (3'UTRs) of axonally localized mRNAs (21). The localization of APC to axonal growth cones depends on KIF3A/B/KAP3 (22), and APC, in turn, is required for the axonal localization and translational regulation of several mRNAs (21). While this suggests that APC might link axonally localized mRNAs to the microtubule-

based transport machinery, direct evidence for this hypothesis has been missing. To address this, we purified (23, 24) fluorescently tagged (25, 26) full-length mouse APC, the KIF3A/B/KAP3 heterotrimer (KIF3ABK), and obtained synthesized β -actin (β act_{wt}) and β 2B-tubulin (β 2Btub_{wt}) mRNA fragments containing APC binding sequences. We then reconstituted APC-mediated mRNA transport in vitro (movie S1) and used a TIRF-M (total internal reflection microscopy) assay (fig. S1A) with single-molecule sensitivity to directly visualize and dissect the machinery and regulatory mechanisms driving mammalian mRNA transport.

RESULTS

APC recruits β 2B-tubulin mRNA to kinesin-2 to form processive mRNA transport complexes

To test whether full-length APC could function as linker between RNAs and kinesins, we first measured the interaction strength between full-length APC–green fluorescent protein (GFP) (fig. S1B) and a minimal β 2Btub-mRNA 3'UTR fragment (β 2Btub_{wtmin}) containing a guanine-rich APC interaction motif (21) (table S1) using microscale thermophoresis (MST; Fig. 1A). In a second experiment, we measured the interaction strength between APC-GFP and KAP3 (Fig. 1B and fig. S1C). Both measured affinities are in the lower nanomolar range, making the assembly of a ternary RNA transport complex a possible scenario. To further test whether these interactions are sufficient to drive processive mRNA transport, we next combined KIF3ABK (fig. S1D), tetramethylrhodamine (TMR)-labeled APC (fig. S1B), and an Alexa647-labeled β 2Btub-mRNA fragment (β 2Btub_{wt}; table S1) in a TIRF-M in vitro motility assay (movie S2). The components assembled into processively moving complexes containing both APC and β 2Btub_{wt} (Fig. 1C).

To assess whether APC is essential for β 2Btub_{wt} transport, we performed experiments with and without APC, resulting in the loss of processive RNA movement in the absence of APC (Fig. 1, D and E). Without the motor protein, APC (movie S3) and APC- β 2Btub_{wt} ribonucleoprotein complexes (APC-RNPs; movie S4) bind and diffuse

Copyright © 2020
The Authors, some
rights reserved;
exclusive licensee
American Association
for the Advancement
of Science. No claim to
original U.S. Government
Works. Distributed
under a Creative
Commons Attribution
NonCommercial
License 4.0 (CC BY-NC).

¹Centre for Genomic Regulation (CRG), The Barcelona Institute of Science and Technology (BIST), Doctor Aiguader 88, Barcelona 08003, Spain. ²Universitat Pompeu Fabra (UPF), Barcelona, Spain. ³ICFO, Castelldefels, Spain.

*Corresponding author. Email: sebastian.maurer@crgeu

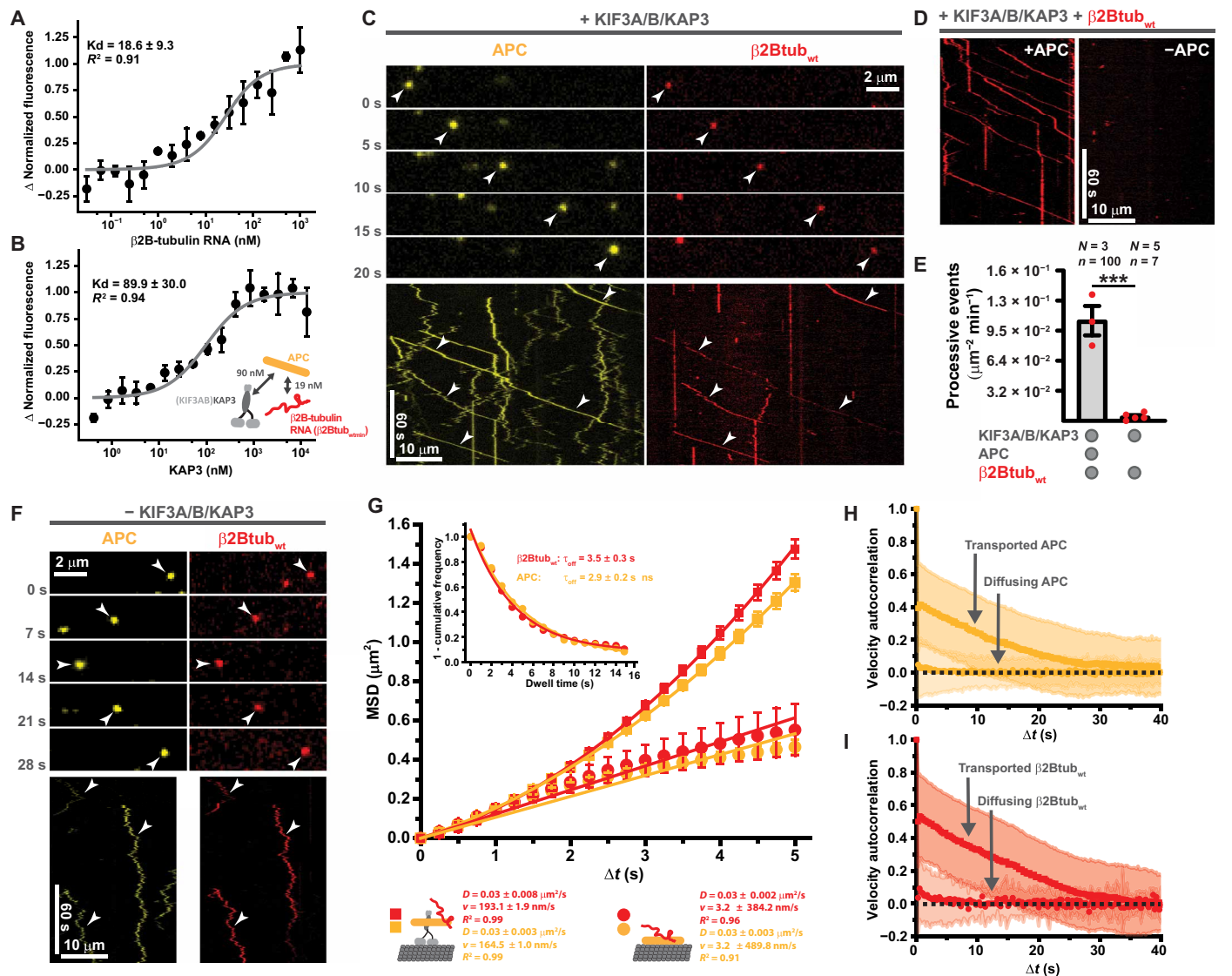


Fig. 1. APC and kinesin-2 are necessary and sufficient to transport β 2Tubulin-mRNA. (A and B) Full-length APC binds KAP3 and β 2Tubulin-RNA (β 2Tub_{wtmin}) with different affinities. Interactions of APC-GFP with β 2Tub_{wtmin} (A) and KAP3 (B) were measured by MST in solution. Inset in (B) shows a summary of affinities measured between RNA transport complex components. Error bars, SD. (C) KIF3ABK transports RNPs containing APC-TMR and Alexa647- β 2Tub_{wt}. Top: Time sequence from a TIRF-M assay containing 750 pM KIF3ABK, 80 pM APC-TMR, and 2 nM Alexa647- β 2Tub_{wt}. Bottom: A kymograph showing multiple run events of APC-TMR and Alexa647- β 2Tub_{wt} complexes, indicated by white arrowheads. (D) APC is essential for β 2Tub_{wt} transport. The kymographs show Alexa647- β 2Tub_{wt} signals from TIRF-M experiments with (left) or without (right) APC. (E) Quantification of processive β 2Tub_{wt} run events in the presence and absence of APC. *N*, number of independent experiments; *n*, total number of events. Error bars, SEM. Statistical significance was evaluated with an unpaired, two-tailed *t* test. ****P* < 0.001. (F) APC recruits β 2Tub_{wt} to the microtubule lattice in the absence of KIF3ABK. Top: Time sequence from a TIRF-M assay containing 40 pM APC-TMR and 2 nM Alexa647- β 2Tub_{wt}. Bottom: Kymographs showing APC-RNA codiffusion events (white arrowheads). (G) MSD plots of APC-TMR and Alexa647- β 2Tub_{wt} from the experiments shown in (C) and (F). Error bars, SEM. Inset, the dwell times of APC-TMR and Alexa647- β 2Tub_{wt} in the absence of KIF3ABK on the microtubule lattice. Statistical significance was evaluated with a Mann-Whitney test on the raw data. (H and I) APC- β 2Tub_{wt} complex lattice diffusion is not biased. Velocity autocorrelations of transported and lattice-diffusing APC-TMR (H) and Alexa647- β 2Tub_{wt} (I) are shown. Error bars, SD.

on the microtubule lattice (Fig. 1F), showing that the reported microtubule binding (19) and RNA binding (21) activities of APC do not exclude each other at a saturating RNA concentration (fig. S1F). This indicates that APC has different binding sites for RNAs and microtubules.

To dissect the different types of motility observed, we next used a single-particle tracking method (27) to create individual trajectories

of diffusing and transported APC-TMR and Alexa647- β 2Tub_{wt} molecules (fig. S1, G and H). To avoid bias, the entire field of view of the entire TIRF-M movies was analyzed. We then computed the mean squared displacement (MSD) (28) of APC and β 2Tub_{wt} signals in dual-color experiments in the presence and absence of KIF3ABK (Fig. 1G), which shows that kinesin addition induces processive movement of APC and β 2Tub_{wt}. Dwell time measurements of diffusing

APC-RNPs in the absence of KIF3ABK, over time frames in which no bleaching occurs (fig. S1, I and J), yield results of nonsignificant difference for APC and $\beta 2\text{Tub}_{\text{wt}}$, indicating that the APC-RNA interaction is more stable than the APC-microtubule interaction (Fig. 1G, inset); if the RNA would dissociate from microtubule-bound APC faster than APC dissociates from the microtubule, one would expect to observe shorter RNA dwell times. A velocity autocorrelation analysis (Fig. 1, H and I) demonstrates that in contrast to transported APC-RNPs, lattice diffusing RNPs do not show any directionality. These experiments reveal that APC couples $\beta 2\text{Tub}_{\text{wt}}$ with high affinity to a kinesin cargo adaptor and microtubules to enable both directed and non-biased diffusive RNA transport.

KAP3 functions as adaptor between kinesin-2 and APC-mRNA complexes

Next, we assessed whether KAP3, which is thought to function as adaptor between APC and the KIF3AB heterodimer (18) (fig. S2A) and which is required for axonal localization of APC (22), is necessary for $\beta 2\text{Tub}_{\text{wt}}$ RNA transport. In the absence of KAP3, directed $\beta 2\text{Tub}_{\text{wt}}$ transport was not detectable, whereas adding back separately purified KAP3 (fig. S1C) to the assay restored processive $\beta 2\text{Tub}_{\text{wt}}$ movement (Fig. 2, A to C). Using size exclusion chromatography coupled multiangle light scattering (SEC-MALS), we confirmed that separately purified KAP3 can interact with KIF3A (fig. S2C) dimers to

form a trimeric complex (fig. S2D). The mean velocity measured for processive (displacement $>4 \mu\text{m}$; fig. S2E) $\beta 2\text{Tub}_{\text{wt}}$ transport complexes was $0.57 \mu\text{m/s}$ (Fig. 2D), which matches the reported velocity for KIF3ABK in cells (29) and in vitro (30) and also the reported velocities for axonally localized RNAs in cultured neurons (11, 31).

APC-RNA complexes activate kinesin-2

Microtubule binding proteins such as APC often function as catalyst for microtubule recruitment and processive movement of kinesins (32–34). APC, harboring an N-terminally localized KAP3-binding site (18) and a C-terminally localized Tau-like microtubule binding site (35), could function as recruitment factor for KIF3ABK. To test this, we purified full-length, heterotrimeric, Alexa647-labeled KIF3ABK (fig. S1D) and tested its activity with in vitro motility assays in the presence and absence of APC (Fig. 2E). Addition of APC triggered microtubule recruitment and processive runs of Alexa647-KIF3ABK, demonstrating that APC functions as kinesin-2 activator in vitro. As RNAs were reported to activate transport of minimal, dynein-based *Drosophila melanogaster* mRNA transport systems (34), we further tested the effect of $\beta 2\text{Tub}_{\text{wt}}$ on motor activation and found that addition of RNA to the APC–kinesin-2 complex further increases transport activation (Fig. 2, E and F, and movie S5). The N and C termini of APC are reported to self-interact (36, 37), and the self-interaction domains of APC span or flank both the KAP3

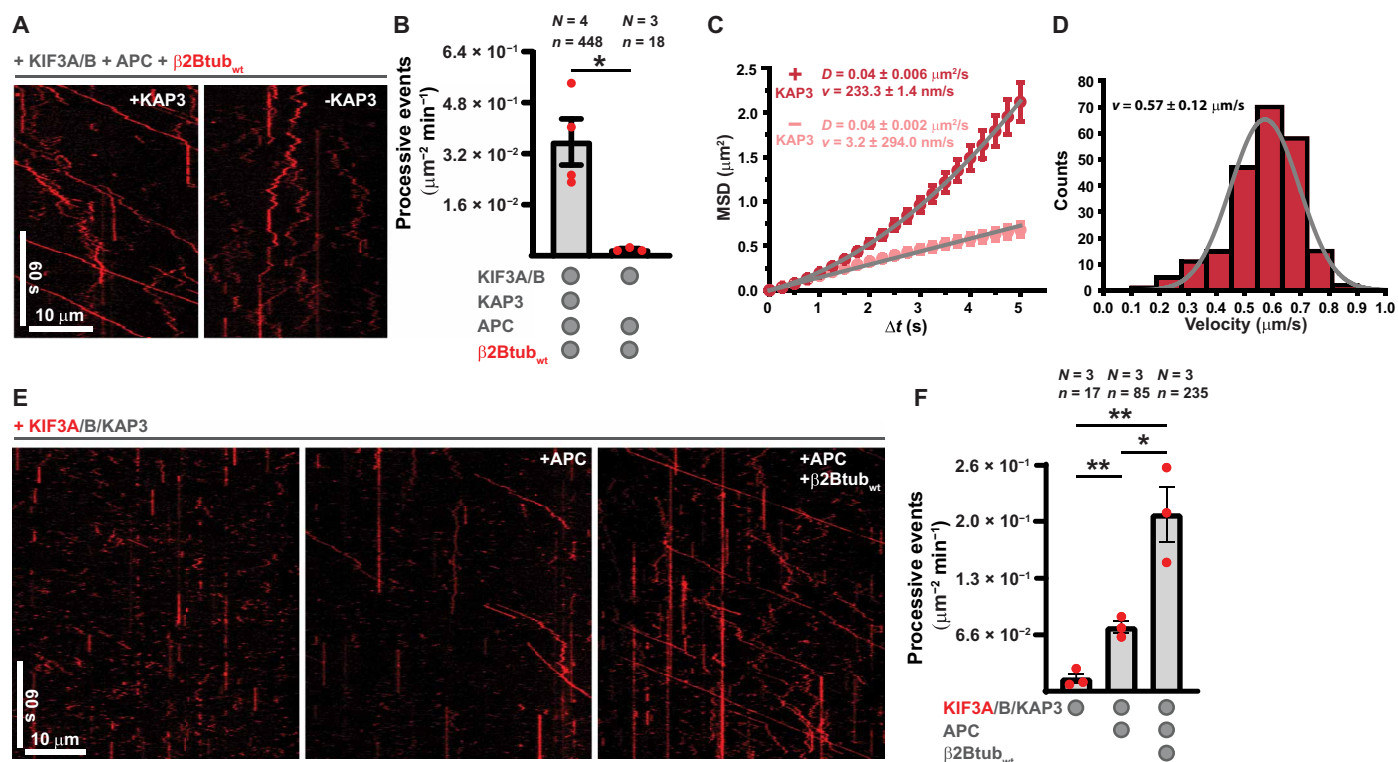


Fig. 2. Function of the individual mRNA transport complex components. (A) KAP3 is required for processive RNA transport. Kymographs show Alexa647- $\beta 2\text{Tub}_{\text{wt}}$ signals from TIRF-M experiments containing 750 pM KIF3AB, 150 pM APC, 2 nM Alexa647- $\beta 2\text{Tub}_{\text{wt}}$, and 500 pM KAP3 (left) or no KAP3 (right). (B) Quantification of processive Alexa647- $\beta 2\text{Tub}_{\text{wt}}$ run events in the presence and absence of KAP3. Error bars, SEM. (C) MSD plots of Alexa647- $\beta 2\text{Tub}_{\text{wt}}$ motility (displacement $>1.1 \mu\text{m}$ to include nonprocessive events in experiments lacking KAP3) from experiments shown in (A). Error bars, SEM. (D) Mean instantaneous velocity distribution of processive (displacement $>4 \mu\text{m}$) Alexa647- $\beta 2\text{Tub}_{\text{wt}}$ complexes. Gray line: A Gauss fit to velocity distribution. (E) APC and $\beta 2\text{Tub}_{\text{wt}}$ activate KIF3ABK. The kymographs show Alexa647-KIF3ABK (750 pM) signals from TIRF-M experiments containing either only KIF3ABK (left) or in addition 80 pM APC (middle) or 80 pM APC and 2 nM TMR- $\beta 2\text{Tub}_{\text{wt}}$ (right). (F) Quantification of processive Alexa647-KIF3ABK run events in the presence and absence of APC or APC- $\beta 2\text{Tub}_{\text{wt}}$ RNPs. Error bars, SEM. In (B) and (F), statistical significance was evaluated with an unpaired, two-tailed *t* test. ** $P < 0.01$, * $P < 0.05$. *N*, number of independent experiments; *n*, total number of events.

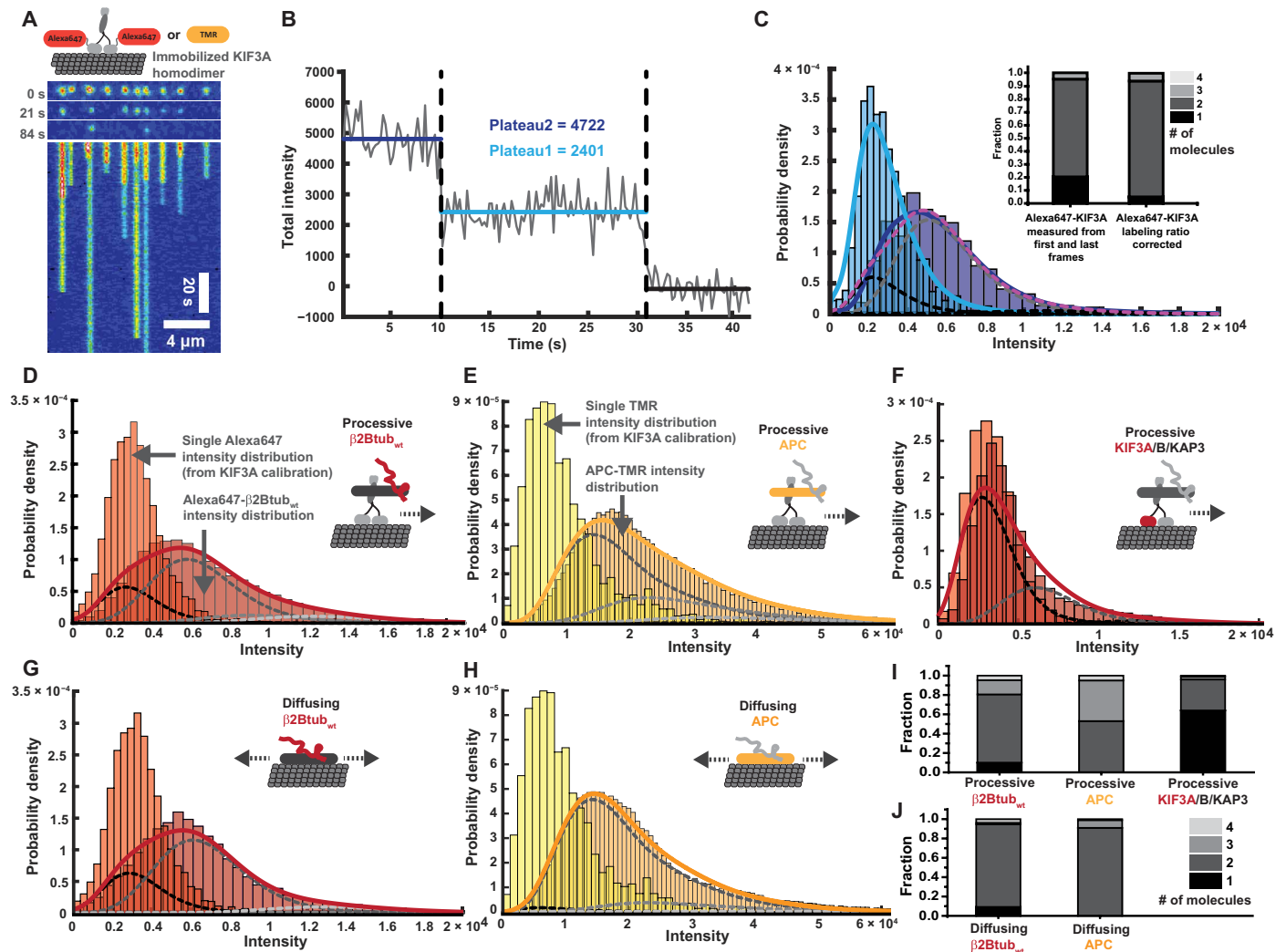


Fig. 3. Fluorescence quantification of motile complexes reveals the mRNA transport complex architecture. (A) Bleaching of an Alexa647-KIF3A homodimer calibration sample. The cartoon on the top schematizes the experimental setup; 10 pM homodimeric SNAP-KIF3A labeled either with Alexa647 or TMR was imaged on paclitaxel-stabilized microtubules in the presence of AMPNP to immobilize the kinesin. The central three images and kymograph at the bottom show an exemplary time course of Alexa647-KIF3A bleaching. (B) A bleaching trace obtained from a single Alexa647-KIF3A dimer indicating total intensities of one and two Alexa647 fluorophores. (C) The blue distributions show total intensities derived from single-particle tracking of immobilized KIF3A-Alexa647 dimers (dark blue, derived from the first 10 s; light blue, derived from the last 20 frames). Correspondingly, the light and dark blue lines indicate kernel density function (KDF) fits to the shown distributions. The dotted magenta line shows the least square fit of the sum of the monomer and multimer fractions (black and gray dotted lines), derived from iterative convolutions of the monomer distribution (light blue line). The inset bar graphs show the measured fraction of KIF3A mono- and multimers and the real fractions obtained after correcting for the labeling ratio of KIF3A (table S2). (D to F) Quantification of molecules in individual RNA transport complex components. Using single-particle tracking, the total intensities of KIF3ABK, APC, and $\beta 2\text{tub}_{\text{wt}}$ was measured in processive (displacement $>4 \mu\text{m}$) complexes. For (D) and (E), experiments contained 750 pM KIF3ABK, 80 pM APC-TMR, and 2 nM Alexa647- $\beta 2\text{tub}_{\text{wt}}$. For (F), experiments contained 750 pM Alexa647-KIF3ABK, 80 pM APC, and 2 nM TMR- $\beta 2\text{tub}_{\text{wt}}$. (G and H) Intensity distributions of microtubule lattice-diffusing RNPs from assays containing 40 pM APC-TMR and 2 nM Alexa647- $\beta 2\text{tub}_{\text{wt}}$. (I) Number of molecules of RNA transport complex components derived from (D) to (F) after labeling ratio (table S2) correction. (J) Number of molecules in diffusive RNPs derived from (G) and (H) after labeling ratio correction. The schematized complexes depicted in (D) to (H) illustrate the experimental setup and the transport complex component analyzed (colored). For (D) to (H), at least three independent experiments were analyzed, providing at least 75 tracks containing $>11,000$ total intensities from detected particles. Light-red or light-yellow distributions show intensity distributions of Alexa647- or TMR-Kif3A from calibration experiments. Colored lines (red or yellow) indicate KDF. Dotted lines indicate monomer and multimer fractions grayscale according to legend in (J).

and the mRNA binding sites. We, hence, speculate that RNA might enhance APC-motor coupling and, hence, transport activation by a potential competition with APC's intramolecular interactions that could make its motor binding region more accessible.

As APC can bind both microtubules and KAP3 with different domains, we finally asked whether APC functions as an allosteric

activator or by recruiting KIF3ABK to the microtubule. To this end, we cloned and purified a fluorescently labeled APC fragment covering only the KAP3-binding APC armadillo domain (APC_{ARM} ; fig. S2F) (18). In TIRF-M experiments, this fragment activated transport and was itself transported (fig. S2G), indicating that the armadillo region is sufficient to bind to KIF3ABK and activate the kinesin to

a comparable extent as full-length APC (fig. S2H). However, as we also observed lattice diffusion of APC_{ARM}, we asked whether this was caused by codiffusion with nonprocessive motors. We next omitted KIF3ABK from the experiments and found that APC_{ARM} is capable of binding and diffusing on microtubules on its own (fig. S2I). Hence, we cannot say with certainty by which mechanism APC activates KIF3ABK.

The reconstituted system transports a low number of mRNAs

In neurons, mRNAs are transported in defined packages containing only a few mRNA molecules (10, 11, 38, 39). The quantity of mRNAs found in mRNA transport complexes is flexible within limits; while the majority of complexes contain one or two of the same mRNAs, a smaller fraction contains more (10, 11). To analyze whether our reconstituted system recapitulates this key property of neuronal mRNA transport complexes and to understand the architecture of our reconstituted transport complexes, we measured the numbers of motor, APC, and RNA molecules in reconstituted β 2B-tubulin RNA transport complexes at a saturating RNA concentration (fig. S1F). As calibration standard to determine single-fluorophore intensities, we used immobilized SNAP-KIF3A (fig. S3, A and B) labeled with either Alexa647 or TMR and first extracted dual- and single-fluorophore intensities from bleaching steps (Fig. 3, A and B). Bleaching step analysis provided a reliable reference for fluorophore brightness but cannot be used to measure the number of molecules in motile transport complexes. Hence, we next confirmed that intensity distributions generated by single-particle tracking of immobilized Alexa647-KIF3A dimers (Fig. 3C) match intensities obtained from bleaching step analysis.

We then used single-particle tracking to measure the total intensities of processively moving Alexa647- β 2Btub_{wt} (movie S6), APC-TMR, and SNAP-KIF3ABK (with only KIF3A being Alexa647 labeled) in experiments in which either the kinesin and RNA or APC and RNA were labeled (Fig. 3, D to F). The same analysis was done for microtubule lattice-diffusing APC-RNPs in the absence of the kinesin (Fig. 3, G and H). We find that, on average, a single KIF3ABK heterotrimer transports one or two APC dimers that carry RNAs at an equal stoichiometric ratio (Fig. 3I). Lattice-diffusing APC is mainly a dimer, which is, on average, bound by one RNA per APC monomer under saturating conditions (Fig. 3J). These results demonstrate that APC and KIF3A/B/KAP3 assemble into RNA transport complexes showing the same confined variability in RNA cargo quantity per transport complex as observed in cells.

APC-kinesin-2 complexes selectively transport several axonal mRNAs

mRNA transport machineries must be selective for a subset of the thousands of expressed mRNAs and, at the same time, balance transport frequencies of different mRNAs despite large differences in expression levels; also, mRNAs present at low copy numbers must be transported. To first test whether our reconstituted system is selective, we conducted experiments with β act (β act_{wt}) and β 2Btub 3'UTR fragments, which carry different variants of the APC binding motifs (21). In addition, we designed RNAs in which APC motifs are mutagenized to contain a low number of guanines. Comparing each wild-type RNA to its mutated version shows that the APC-RNA transport system is selective (movies S7 and S8), giving clear preference to the wild-type RNAs in both cases (Fig. 4, A and B). At the same time these experiments show that APC can link different G-motif-containing RNA sequence found in axonal mRNAs to kinesin-2.

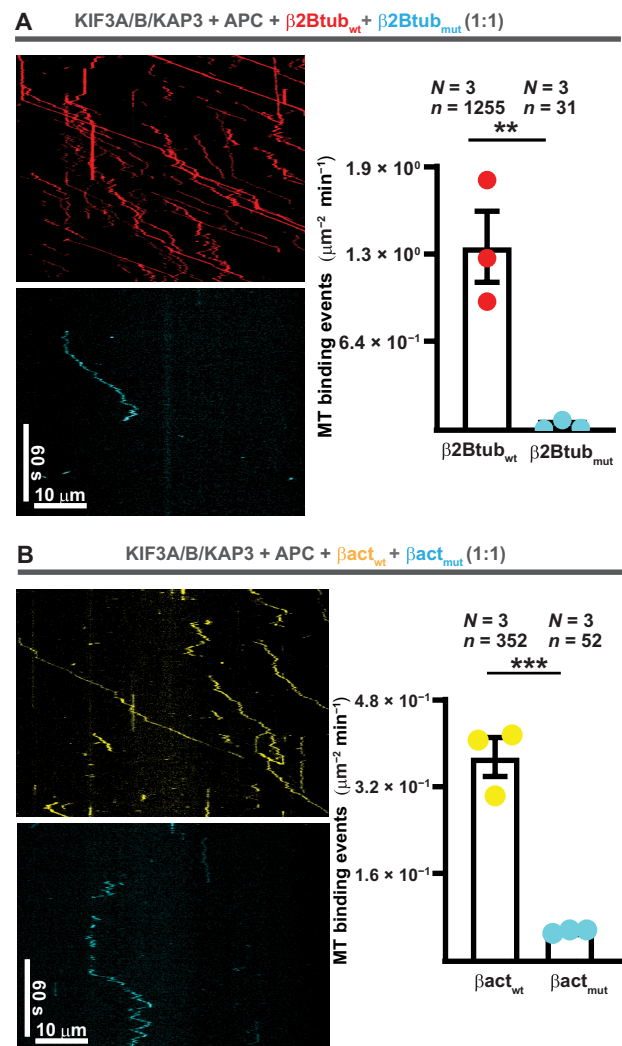


Fig. 4. APC selectively links β -actin and β 2B-tubulin mRNAs to kinesin-2. (A) Kymographs showing Alexa647- β 2Btub_{wt} and TMR- β 2Btub_{mut} in experiments containing 750 pM KIF3ABK and 150 pM APC. Equimolar RNA concentrations of 500 pM were used. Right: Quantification of Alexa647- β 2Btub_{wt} and TMR- β 2Btub_{mut} microtubule binding events (diffusive and processive). (B) Same as in (A) but comparing TMR- β actin_{wt} to Alexa647- β actin_{mut} RNA using equimolar RNA concentrations of 3000 pM. Right: Quantification of TMR- β actin_{wt} and Alexa647- β actin_{mut} microtubule binding events (diffusive and processive). Error bars in (A) and (B), SEM. In (A) and (B), statistical significance was evaluated with an unpaired, two-tailed t test. *** P < 0.001, ** P < 0.01.

Different affinities of APC to different mRNAs fine-tune mRNA transport frequency

As β -actin mRNA is at least 10-fold more abundant than β 2B-tubulin mRNA in cortical and hippocampal neurons (40), we next asked how an mRNA transport system compensates for different cargo concentrations in a situation of competition. At a 10-fold excess of β act_{wt} over β 2Btub_{wt}, both RNAs are transported (Fig. 5A). Decreasing β 2Btub_{wt} concentrations, while keeping the β act_{wt} concentration constant, increases the fraction of β act_{wt} bound to microtubules in an APC-dependent manner (diffusive and processively transported; Fig. 5B). Analyzing the total number of processive β act_{wt} transport events showed that more β act_{wt} is transported with decreasing β 2Btub_{wt} concentrations (Fig. 5C and movie S9). While the dwell times of both

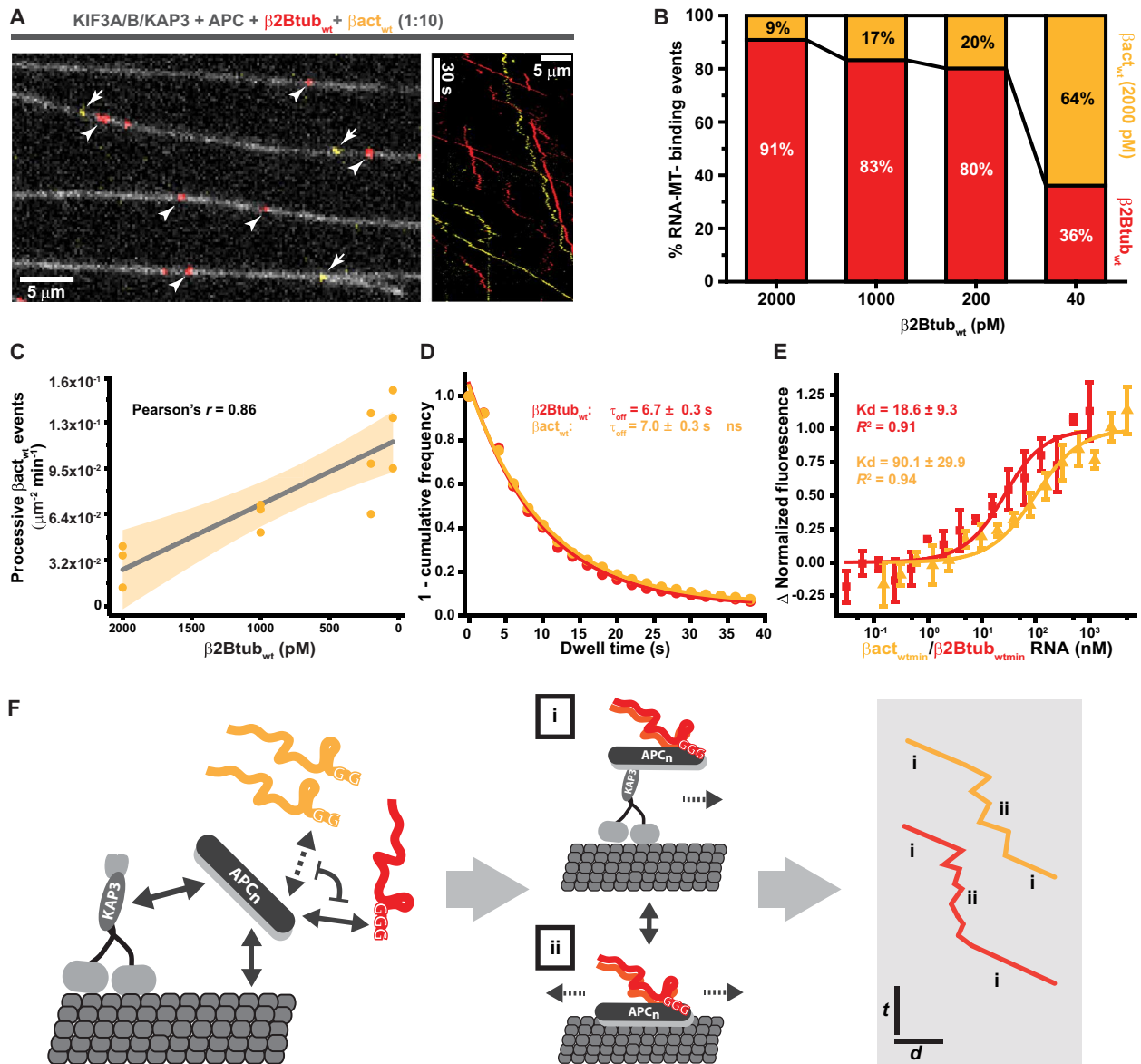


Fig. 5. The affinity of APC to different mRNAs controls mRNA transport frequency. (A) An overview TIRF-M image (left) and kymograph (right) showing Alexa647- $\beta 2\text{Tub}_{\text{wt}}$ and TMR- $\beta\text{act}_{\text{wt}}$ transport in the same experiments at 1:10 molar ratio (200 pM:2 nM). Arrows and arrowheads point to TMR- $\beta\text{act}_{\text{wt}}$ and Alexa647- $\beta 2\text{Tub}_{\text{wt}}$ RNPs, respectively. (B) A titration of Alexa647- $\beta 2\text{Tub}_{\text{wt}}$ from 2000 to 40 pM leads to an increase in the relative amount of TMR- $\beta 2\text{Tub}_{\text{wt}}$ transport per experiment. (C) Plot of processive run events of TMR- $\beta\text{act}_{\text{wt}}$ (displacement $>4 \mu\text{m}$) per experiment in dependence of the free Alexa647- $\beta 2\text{Tub}_{\text{wt}}$ concentration. Gray line: Linear regression fit. Yellow-shaded area: 95% confidence band. (D) Dwell time distribution of $\beta 2\text{Tub}_{\text{wt}}$ and $\beta\text{act}_{\text{wt}}$ RNAs in experiments containing 750 pM KIF3ABK, 150 pM APC, 40 pM Alexa647- $\beta 2\text{Tub}_{\text{wt}}$ and 2000 pM TMR- $\beta\text{act}_{\text{wt}}$. Colored solid lines: Monoexponential decay fits to dwell time distributions. (E) MST measurement of the affinity of $\beta\text{act}_{\text{wt}}$ and $\beta 2\text{Tub}_{\text{wt}}$ RNA to APC-GFP. Error bars, SD. Solid lines: One-site binding model fit to the measured normalized fluorescence. (F) Model of transport RNP assembly. Oligomerizing APC binds guanine-rich motifs located in mRNA 3'UTRs, microtubules and KAP3 with different domains. mRNAs with different G-motif variants compete for APC binding. APC-RNPs move by two different modes: (i) active transport by kinesin-2 and (ii) microtubule lattice diffusion. In (D), statistical significance was evaluated with a Mann-Whitney test on the raw data. N , number of independent experiments; n , total number of events.

RNAs in the transport complexes do not show a significant difference (Fig. 5D), indicating that again RNA off rates are controlled by motor or APC off rates, the dwell time measured was twice as high compared with what we measured for lattice-diffusing APC-RNPs (Fig. 1G, inset). This potentially stems from the additional microtubule attachment point KIF3ABK provides for APC. To further test

what causes the observed preference of our reconstituted system for $\beta 2\text{Tub}_{\text{wt}}$ RNA, we conducted MST experiments with both RNAs and found that $\beta\text{act}_{\text{wt}}$ had a fivefold lower affinity to APC than $\beta 2\text{Tub}_{\text{wt}}$ (Fig. 5E). These results show that APC has different affinities to different mRNA localization signals, which fine-tunes transport frequencies of different axonally localized mRNAs.

DISCUSSION

Our results show that APC selectively links RNAs with guanine-rich sequences found in the 3' UTRs of mRNAs to the heterotrimeric kinesin-2 KIF3A/B/KAP3. APC's microtubule, RNA, and KAP3 binding activities recruit the heterotrimeric kinesin-2 to the microtubule and trigger the assembly of processive and diffusive mRNA transport complexes (Fig. 4F). While APC is able to activate transport on its own, RNA addition stimulates motor activation further. While more work is required to understand kinesin-2 activation by APC-RNPs, it is conceivable that RNA binding interferes with APC's ability to self-interact; this could lead to an open conformation of APC, which improves interaction with KAP3, thereby enhancing transport. Our experiments with the minimal APC_{ARM} fragment cannot show whether APC activates kinesin-2 by allosteric activation or recruitment to microtubules. Notably, also other MAPs were shown to activate kinesins by both allosteric activation and microtubule recruitment (34). Given the size and domain architecture of APC, it could well be that kinesin-2 activation by APC follows the same principle.

We observe a mixture of pause events, diffusive and directed motion of APC-RNPs, which was also observed for β -actin mRNA in neurons (10, 11, 41). Being able to switch from one transport mode to the other can be of advantage; diffusion is faster than directed transport over shorter distances, it is not affected by microtubule orientation, and it allows switching of protofilament tracks on microtubules to navigate around roadblocks (42). Furthermore, transport events containing pauses and motile phases, as seen for RNPs in neurons and in our reconstituted system, belong to the characteristics of a Lévy walk, a movement pattern that was recently proposed to optimize target search efficiency of synapse-patrolling mRNPs (43).

Axonal APC transport relies on both kinesin-1 and heterotrimeric kinesin-2 (22). Hence, it will be of interest in the future to test whether kinesin-1 can also transport APC-RNPs. This would hint toward an evolutionary conserved mechanism, as also in *Xenopus laevis* oocytes Vg1 mRNA transport depends on the same kinesins (44).

Our stoichiometric analysis of single reconstituted mRNA transport complexes reveals that mostly one to three RNAs are found in one complex at a saturating RNA concentration. Our data match the numbers of the same mRNAs found in neuronal mRNA transport complexes, but we detect a smaller fraction of single-RNA complexes (10, 11). This could be because it is technically challenging to measure RNA labeling ratios both in vitro and in cells. APC's oligomerization domains provide the means to pack different numbers of APC-RNA complexes onto a kinesin, potentially providing a mechanism for cargo concentration-driven loading of transport complexes and for the confined variability of RNA copy number per complex. At the same time, cellular signaling events could modify the self-association abilities of APC to trigger unloading of cargo-mRNAs (36).

Our finding that different guanine sequence variants present in β -actin and β 2B-tubulin mRNAs lead to different transport efficiencies opens an interesting conceptual framework for the evolution of mRNA transport signals; subtle sequence variations might balance the access of mRNAs to the transport system to guarantee transport also of low-abundant mRNAs. Transport motif-mediated fine-tuning of mRNA on and off rates to adaptors such as APC might be one mechanism contributing to the generation of different mRNA distributions observed in neurons (4). Notably, the guanine-rich APC binding sequences resemble G-quadruplex structures known to be a target for FMRP (fragile X mental retardation protein), another RNA-binding

protein involved in neuronal mRNA transport (45). Hence, APC and FMRP are potentially components of partially redundant mRNA transport pathways.

The availability of functional full-length APC for in vitro studies now opens the door to understanding how APC integrates the signals it receives and the many activities it controls such as regulation of microtubule assembly (46), actin nucleation (47), microtubule-actin coordination (48), mRNA localization (6), and translation regulation (21). The identification of the first minimal, mammalian mRNA transport system and the development of an assay system to study mammalian mRNA transport in vitro now provide the means to dissect the molecular mechanisms of different mRNA transport pathways and to understand how their interplay generates the observed mRNA distributions in different cell types.

MATERIALS AND METHODS

Materials

Chemicals were obtained from Sigma if not stated otherwise. Single-fluorophore, 5'-end-labeled RNA fragments from mouse β -actin mRNA (accession no. NM_007393.5) and mouse β 2B-tubulin mRNA (accession no. NM_023716.2) were purchased from IBA Lifesciences (Germany).

TIRF microscopy experiments were performed on an iMIC (TILL Photonics, Germany) TIRF microscope equipped with three Evolve 512 EMCCD cameras (Photometrics, UK), a 100 \times 1.49 numerical aperture objective lens (Olympus, Japan), a quadband filter (405/488/561/64, Semrock, USA), and four different laser lines (405, 488, 561, and 639 nm). An Olympus tube lens adds a postmagnification of $\times 1.33$, which results in a final pixel size of 120.3 nm.

Methods

Cloning and recombinant protein expression

Sequences encoding APC, KAP3, KIF3A, and KIF3B proteins (*Mus musculus* APC, accession no. AAB59632; *M. musculus* KAP3A, accession no. BAA08901.1; *M. musculus* KIF3A, accession no. NP_032469.2; and *M. musculus* KIF3B, accession no. NP_032470.3) were synthesized commercially and codon optimized for expression in insect cells (Thermo Fisher Scientific). Polymerase chain reaction (PCR)-amplified APC was inserted by Gibson assembly into a pCoofy27 (23) backbone for N-terminal fusion of 10xHis-ZZ-TEV and, if required, C-terminal fusion of mGFP (26) or SNAP tag (26). A similar strategy was applied to obtain 9xHis-ZZ-SUMO-KAP3 and 9xHis-ZZ-SUMO-KIF3A, which were inserted into pCoofy17a (23). KIF3A was N-terminally fused to 6xHis-ZZ-HRV3C and C-terminally to a TEV (Tobacco Etch Virus nuclear-inclusion-a endopeptidase) cleavage site followed by a linker sequence ("HL-linker," ILGAPS-GGGATAGAGGAGGPAGLIN) and SNAP tag. KIF3B was fused to the N-terminal tags OneStrep-ZZ-HRV3C-mGFP-HL-linker-TEV. Proteins were cloned downstream of the *polh* promoter into pLIB (library) vectors, and either KIF3A and KIF3B or KIF3A, B, and KAP3 were combined by Cre/loxP recombination (24). PCR-amplified APC_{ARM} (nucleotides 1008 to 3048 of APC) was inserted by Gibson assembly into a pCoofy17 backbone for N-terminal fusion of ZZ-3C and C-terminal fusion to TEV-HL-linker-SNAP-3C-Strep. For expression of heterodimeric KIFA/B and heterotrimeric KIF3A/B/KAP3, we used the biGBac system (24). All constructs were validated by sequencing of the entire open reading frame. Following expression in SF21 cells, cell pellets were frozen in liquid N₂ and stored at -80°C . For

expression of recombinant proteins in *Escherichia coli* (KAP3 and APC_{ARM}), plasmids were transformed in BL21-AI One Shot chemically competent *E. coli* (Thermo Fisher Scientific, C607003). Overexpression was done at 18°C ON after induction with 0.2% arabinose and 0.5 mM IPTG (isopropyl-β-D-thiogalactopyranoside) at OD₆₀₀ 0.4. Pelleted cells were frozen in liquid N₂ and stored at -80°C until purification.

Protein biochemistry

APC purification. Cold APC purification buffer [100 mM NaPi, Sigma #S3139 and Sigma #S9390, 300 mM KCl, Sigma #P9333, 5 mM MgCl₂ × 6 H₂O, Sigma #M2670, 0.001% Brij35 Thermo Fisher Scientific, #28316, 2.5 mM dithiothreitol (DTT), Sigma #D0632, 2.5 mM EDTA, Sigma #EDS] supplemented with protease inhibitors (Roche, #5056489001) and deoxyribonuclease I (DNaseI) (Roche, #10104159001) was added to frozen SF21 cell pellets expressing an APC construct. The pellet was thawed in a room temperature water bath and resuspended. The lysate was clarified by centrifugation (184,000g, 45 min, 4°C), and the supernatant was applied to a 5-ml HiTrap immunoglobulin G Sepharose FF column (GE Healthcare, #28-9083-66). After washing with APC purification buffer, GST (glutathione S-transferase)-TEV protease was added to the column, and the column was left at 4°C overnight to cleave APC off its column-bound affinity and solubility tags. The next day, APC was eluted with APC purification buffer and labeled with SNAP-reactive dye (NEB #S9105). After SNAP labeling, APC was concentrated using Vivaspin concentrators (Sartorius), ultracentrifuged (280,000g, 10 min, 4°C), and gel filtered using a Superose6 10/300 GL column (GE Healthcare). Peak fractions were pooled, and the labeling ratio was determined using NanoDrop (Thermo Fisher Scientific). The protein was aliquoted on ice and snap frozen in liquid nitrogen.

KIF3A/B/(KAP3) purification. Cold KIF3A/B purification buffer (80 mM NaPi, 200 mM KCl, 5 mM MgCl₂ × 6 H₂O, 0.001% Brij35, 2.5 mM DTT, 2.5 mM EDTA, and 0.1 mM ATP, #A2383) supplemented with protease inhibitors and DNaseI was added to frozen SF21 cell pellets expressing a KIF3A/B construct. Thawing and lysate clearing were done as described for APC purification above. Next, the supernatant was applied to a StrepTrap column (GE Healthcare, 28-9075-48). The column was washed with KIF3A/B purification buffer, and the protein was eluted in KIF3A/B purification buffer supplemented with 15 mM *d*-desthiobiotin (Sigma, D1411-1G). Depending on whether unlabeled or fluorescently tagged protein was needed, the eluate was incubated either with TEV and 3C or only 3C protease overnight at 4°C. After SNAP labeling, the protein was concentrated and ultracentrifuged as described above and gel filtered using a GE Superdex200 10/300 column. Peak fractions were pooled, the labeling ratio was determined using NanoDrop. The protein was aliquoted on ice and snap frozen in liquid nitrogen.

KIF3A purification. Cold KIF3A purification buffer (50 mM NaPi, 400 mM KCl, 2 mM MgCl₂ × 6 H₂O, 0.001% Brij35, 0.75 mM β-mercaptoethanol, Sigma #M3148, and 0.2 mM ATP) supplemented with protease inhibitors and DNaseI was added to frozen BL21-RIL cell pellets expressing a KIF3A construct. Pellets were thawed and sonicated. The lysate was clarified by centrifugation (184,000g, 45 min, 4°C), and the supernatant was applied to a 5-ml HiTrap column (GE Healthcare) loaded with cobalt(II)-chloride hexahydrate (Sigma #255599). The column was washed with KIF3A purification buffer, and the protein was eluted in KIF3A purification buffer supplemented with 500 mM imidazole (Sigma #I2399). The eluate was concentrated with a Vivaspin concentrator (Sartorius) and supplemented with 8 mM β-mercaptoethanol. Affinity tags were cleaved overnight at 4°C using

SUMO protease. In the case of KIF3A-SNAP, the protein was concentrated after labeling using a Vivaspin concentrator (Sartorius), ultracentrifuged (280,000g, 15 min, 4°C), and gel filtered using a GE Superdex200 10/300 GL column. Peak fractions were pooled, and the labeling ratio was determined using NanoDrop. The protein was aliquoted on ice and snap frozen in liquid nitrogen.

KAP3 purification. Cold KAP3A purification buffer [50 mM Hepes, Sigma #H3375, 400 mM KCl, 2 mM MgCl₂, 0.002% Brij35, 1 mM β-mercaptoethanol, 1 mM imidazole, 50 mM L-arginine, Sigma #A5006, and 50 mM L-glutamate, Sigma #49449 (pH 7.25)] supplemented with protease inhibitors and DNaseI was added to frozen BL21-AI cell pellets expressing a KAP3A construct. Pellets were thawed and cells were lysed by French press at 10,000 psi. The lysate was clarified by centrifugation (184,000g, 45 min, 4°C), and the supernatant was applied to a 5-ml HiTrap column (GE Healthcare) loaded with cobalt(II)-chloride hexahydrate (Sigma). The column was washed with KAP3A purification and buffer containing 10 mM imidazole, and the protein was eluted in KAP3A purification buffer supplemented with 400 mM imidazole. The eluate was concentrated with a Vivaspin concentrator (Sartorius) and supplemented with 8 mM β-mercaptoethanol. Affinity tags were cleaved overnight at 4°C using SUMO protease. KAP3A was concentrated using a Vivaspin concentrator (Sartorius), ultracentrifuged (280,000g, 15 min, 4°C), and gel filtered using a GE Superdex200 10/300 GL column. Peak fractions were pooled, and the protein was aliquoted on ice and snap frozen in liquid nitrogen.

APC_{ARM} purification. Cold APC purification buffer (100 mM NaPi, Sigma #S3139 and Sigma #S9390, 300 mM KCl, Sigma #P9333, 5 mM MgCl₂ × 6 H₂O, Sigma #M2670, 0.001% Brij35 Thermo Fisher Scientific #28316, 2.5 mM DTT, Sigma #D0632, and 2.5 mM EDTA, Sigma #EDS) supplemented with protease inhibitors (Roche, #5056489001) and DNaseI (Roche, #10104159001) was added to frozen *E. coli* cell pellets expressing an APC-ARM construct. The pellet was thawed and resuspended. The lysate was clarified by centrifugation (184,000g, 45 min, 4°C), and the supernatant was applied to a StrepTrap column (GE Healthcare, 28-9075-48). The column was washed with APC purification buffer, and the protein was eluted in APC purification buffer supplemented with 10 mM *d*-desthiobiotin (Sigma, D1411-1G). Next day, the protein was incubated with 3C protease (Speed Biosystems, YCP1208) for 1 hour at 16°C. After SNAP labeling, the protein was concentrated and ultracentrifuged as described above and gel filtered using a GE Superdex200 10/300 column. Peak fractions were pooled, and the labeling ratio was determined using NanoDrop. The protein was aliquoted on ice and snap frozen in liquid nitrogen.

SNAP labeling of proteins

SNAP labeling was carried out at 15°C for 90 min using threefold excess of dye over protein before gel filtration. Fresh DTT (2 mM) was added directly before labeling. Unbound dye was immediately removed using Zeba Spin desalting columns (Thermo Fisher Scientific).

SDS-PAGE and Western blotting

SDS-polyacrylamide gel electrophoresis (PAGE) was performed using Mini-Protean system and TGX precast gels (Bio-Rad). Proteins were stained with BlueSafe solution (Nzytech). Western blotting on SDS gels was performed with an Invitrogen iBlot2 device and fitting iBlot2 NC stacks (Invitrogen). The antibody for KAP3 detection was purchased from Santa Cruz Biotechnology (sc-55598 HRP).

Reproducibility

At least three independent experiments were performed for all tested conditions.

MST measurements

MST experiments were carried out with a Monolith NT.115 system (Nanotemper, Germany). APC-GFP (15 nM) was titrated on ice with increasing concentrations of KAP3 (13,450 to 0.41 nM), β act_{wtmin} (5000 to 0.15 nM), or β 2Tub_{wtmin} (1000 to 0.03 nM) in a final assay buffer: 25 mM tris (pH 7.4), 75 mM NaCl, 5 mM MgCl₂, and 0.025% Tween 20. RNA assay buffer was supplemented with 0.125 U SuperaseIn (Invitrogen) and 2.5 mM EDTA. Sixteen PCR tubes were filled with a 1:2 dilution of the titrants, and a constant amount of APC-GFP was added. Tubes were shifted to room temperature, and mixtures were transferred to 16 standard capillaries (Nanotemper, Germany) according to the manufacturer's manual, which were allowed to equilibrate for 4 min at 30°C before measurement. Data were acquired using 40% MST and 50% light-emitting diode (blue filter) power. Binding curves were obtained by plotting the fluorescent change 5 s after applying the MST gradient against the concentration of the titrated protein or RNA. Data from three replicates were averaged and fitted with a Kd model derived from the law of mass action

$$(49): y = A1 + \frac{(A2 - A1) * (fc + x + kd - \sqrt{(fc + x + kd)^2 - 4 * fc * x})}{2 * fc}$$

The concentration of the fluorescent molecule (*fc*, APC-GFP in our case) is constant at 15 nM, while *x* corresponds to the concentration of the titrated ligand. A1 and A2 correspond to the normalized fluorescence value of the unbound and bound states, respectively.

SEC-MALS measurements

Storage buffer of KIF3A and KAP3 was exchanged against SEC-MALS buffer (30 mM Hepes, 200 mM KCl, 2 mM MgCl₂, 10 mM β -mercaptoethanol, and 0.05% NaN₃) with Zeba Spin desalting columns (Thermo Fisher Scientific). Proteins were resolved either separately or after mixing KIF3A with KAP3 in a 2:1 molar ratio on a Shodex KW-804 column (Shodex, Germany). Following SEC fractionation, eluted protein was detected on a Wyatt Dawn 8⁺ eight-angle light scattering instrument coupled to a Wyatt Optilab T-rEX on-line refractive index detector in a standard SEC-MALS format.

Polymerization and stabilization of microtubules

Microtubules were polymerized from bovine tubulin with stochastic incorporation of ATTO390 (Attotech, Germany) and biotin-labeled tubulin (Thermo Fisher Scientific, #20217). Mixes of 36 μ M unlabeled tubulin, 14 μ M ATTO390-tubulin, and 10 μ M biotin-tubulin were incubated in BRB80 [80 mM PIPES (pH 6.85), 2 mM MgCl₂, and 1 mM EGTA] with 4 mM GTP (Sigma) for 25 min at 37°C in a total volume of 25 μ l. Next, prewarmed BRB80 supplemented with 20 μ M paclitaxel (Sigma) was added, and incubation continued for 45 min at 37°C. Polymerized microtubules were pelleted at 20,000g for 5 min and resuspended in 50 μ l BRB80 supplemented with 20 μ M paclitaxel.

Motility chamber preparation

Glass surfaces were prepared as described previously (50). Motility chambers with a volume of ~10 μ l were assembled by adhering glass cover slips functionalized with polyethylene glycol (PEG) and biotin-PEG [Microsurfaces Inc., USA, #Bio_01(2007134-01)] to glass slides passivated with PLL(20)-g[3.5]-PEG (2) (SuSos AG, Duebendorf, Switzerland) using two parallel segments of double-sided adhesive tape. Chamber surfaces were passivated for 5 min on ice with 5% (w/v) Pluronic F-127 (#P2443) in TIRF-M assay buffer [90 mM Hepes, 10 mM Pipes #P6757, 2.5 mM MgCl₂, 1.5 mM EGTA #03777, and 15 mM β -mercaptoethanol (pH 6.9)] supplemented with kappa-casein (50 μ g/ml; #C0406). Chambers were then flushed with neutravidin (25 μ g/ml; Invitrogen, #A-2666) in assay buffer containing kappa-

casein (200 μ g/ml) and instantly rinsed with assay buffer followed by warm up to room temperature. After 3 min, microtubules were diluted 1:15 in room temperature assay buffer and added to the chamber followed by 3 min of incubation.

In vitro motility assay

Constituents of motility assays were incubated on ice for 15 min in TIRF-M assay buffer supplemented with 4% PEG-3350 #1546547, 2.5 mM ATP, and SuperaseIn (0.5 U/ μ l; Invitrogen, AM2694). Typical protein concentrations were as follows: 10.5 nM APC, 52.5 nM KIF3ABK, and 140 nM RNA. The preincubation mix was diluted 69.89-fold into final motility buffer lacking RNase inhibitor and containing additional glucose oxidase (0.32 mg/ml; AMSBIO, Germany, #22778.02), catalase (0.275 mg/ml; #C40), 50 mM glucose (#G7021), beta-casein (50 μ g/ml; #C6905), and 0.12% methylcellulose (#M0512). Exact final protein and RNA concentrations are given in figure legends. Diluted mixes were applied to immobilized microtubules in the motility chamber for imaging at room temperature (30 \pm 1°C).

TIRF microscopy

For triple color imaging, two channels were recorded alternating, either with two or four frames per second (250- or 125-ms exposure per channel) by switching laser lines 561 and 639 nm. ATTO390 microtubules were recorded as a single image after time lapse movies had been finalized. This protocol was chosen since ATTO390 bleaches comparably fast, and total illumination time per cycle is saved to increase the frame rate in the other channels. For quadruple color imaging, 488- and 639-nm laser lines were switched on simultaneously and alternated with the 561-nm laser line, followed by a single image of ATTO390 MTs at the end. Laser powers as well as exposure times and acquisition frame rates were kept constant within a set of experiments and corresponding calibration samples to allow for direct comparisons between different conditions. For channel alignments, images with 100- μ m TetraSpeck fluorescent beads (Invitrogen, UK) were recorded in all channels before experiments were started.

Analysis of TIRF-M data

For analysis of dynamic properties and the stoichiometry of APC-RNA complexes (APC-RNPs), TIRF-M movies were loaded into the FIJI software (51) and analyzed using Trackmate (27). In all cases, entire TIRF movies including the entire field of view were analyzed to guarantee an unbiased analysis. Single particles were detected using the LoG (Laplacian of Gaussian) detector with an estimated spot diameter of 900 nm. Intensity thresholds for spot detection depended on the amount of fluorescent species used in the respective experiments and were kept constant for all comparisons of experiments using the same concentrations of fluorescent proteins or RNAs and the same imaging settings. To compute trajectories, we used the "Simple LAP tracker" with the following settings: maximal linking distance, 500 nm; maximal gap-closing distance, 500 nm; and maximal frame gap, 4. To read out intensities of stationary KIF3A-Alexa647 and KIF3A-TMR calibration probes used in Fig. 3, a track duration cutoff of >3 s was used to exclude blinking events and transient, non-specific binding. For the analysis of kinesin-2, APC, and RNA dynamics [Figs. 1, G (inset) to I; 2C; 3, G and H; and 4, A, B, D, and F], trajectories with a displacement of >1100 nm were used to analyze only diffusing and processive particles and exclude stationary events that likely arise due to unspecific interactions. As APC-dependent microtubule lattice diffusion never showed a displacement >4000 nm (fig. S2E), this value was used as cutoff when only processive complexes had to be analyzed in Figs. 1 (H and I), 2D, 3 (D to F), and 4 (E and F, inset). The background fluorescence of TIRF-M data

was measured by calculating the mean intensity in a 28×18 pixel rectangular box at five different positions (upper left and right, center, and lower left and right) of the field of view at four different time points of the movie. The obtained mean background fluorescence was subtracted from total spot intensities obtained by Trackmate single-particle tracking. We further always analyzed the entire field of views of entire TIRF-M movies in all cases to exclude bias.

Analysis of transport-RNP dynamics

Trajectories of APC, RNA, and motors obtained from Trackmate processing of TIRF-M data were further analyzed using the MSD analyzer toolbox for MATLAB to compute the MSD and the velocity autocorrelation (28). To compare RNP movements with and without kinesin-2, we fitted the equation $MSD = v^2 t^2 + 2Dt$ assuming a mixed motion of single particles due to APC-induced microtubule lattice diffusion and directed transport. For MSD analysis, in all figures, a displacement cutoff of >1100 nm was used. To test for directed motion of APC-RNA complexes, the velocity autocorrelations of diffusing (displacement cutoff >1130 nm) and transported (displacement cutoff >4000 nm) APC-RNPs were compared in the absence or presence of the kinesin, respectively. For random diffusion, the individual displacement vectors of a track are uncorrelated, resulting in a V_{corr} value of zero. In the case of directed motion, subsequent displacement vectors are comparable, resulting in a V_{corr} value above zero. To analyze dwell times of APC and β 2B-tubulin RNA, 1-cumulative frequency distributions of the respective dwell times (=track duration) were fitted to the monoexponential decay function $y = y_0 + Ae^{-x/\tau}$. The decay constant τ was derived by $\tau = t * \ln(2)$. The mean velocity of RNA transport complexes was determined by computing the average of 224 individual mean track velocities. The mean track velocity is the mean of the instantaneous velocities of a track.

Measurement of single-fluorophore intensities on immobilized samples

To obtain intensities of single and multiple Alexa647 and TMR dyes under conditions comparable to RNA transport assays, we used homodimeric KIF3A-SNAP labeled with either Alexa647 or TMR. The motor was washed into TIRF-M assay chambers in imaging buffer containing 5 mM AMPPNP (adenylyl imidodiphosphate) to induce strong coupling to the immobilized paclitaxel-stabilized microtubules. To allow bleaching, the amount of glucose in the imaging buffer was reduced from 50 to 1 mM. Then, movies were recorded using identical imaging settings as used for RNA transport experiments until most of the fluorophores were bleached. Intensities were obtained from the first 10 frames (multimeric signal) or the last 20 frames (monomeric, single fluorophore signal) using total intensity counts obtained from Trackmate as described above. To detect single-step photobleaching events, the Fiji plugin TimeSeries V3_0 analyzer was used, and intensity time tracks were processed in MATLAB using a custom-written change point detection algorithm to identify intensity plateaus indicative for monomeric or multimeric signals.

Determination of RNA transport complex stoichiometries

To measure the intensity distribution of lattice-diffusing APC-RNA complexes and APC-RNA transport complexes, four different experiments were conducted. For lattice-diffusing APC-RNA complexes, 40 pM APC-GFP and 2000 pM Alexa647- β 2Btub_{wt} were used. To measure the stoichiometry of processive RNA transport complexes, protein concentrations in the TIRF-M assays were as follows: for KIF3A/B/KAP3 intensity measurements, 750 pM Alexa647-KIF3A/B/KAP3, 80 pM APC, and 2000 pM TMR- β 2Btub_{wt} were used. For APC intensity measurements, 750 pM KIF3A/B/KAP3, 80 pM APC-

TMR, and 2000 pM Alexa647- β 2Btub_{wt} were used. For RNA intensity measurements, 750 pM KIF3A/B/KAP3, 80 pM APC, and 2000 pM Alexa647- β 2Btub_{wt} were used. Imaging was done with triple-color mode at four frames per second (described above). Kinesin, APC, and RNA intensities were then obtained from Trackmate analysis, and background intensities were subtracted as described above. Using a custom-written MATLAB script, we calculated the probability density function (kernel density estimation) for both the monomeric intensity distribution (obtained from Alexa647-KIF3A or TMR-KIF3A bleaching experiments, pdf_{mono}) and the intensity distributions of RNA transport complex components (pdf_{RNP}). In general, intensity distributions of Alexa647 and TMR fluorescent molecules are typically right skewed and broader than Poissonian distributions with $std \sim \sqrt{N}$, N the number of photons in the signal. The pdf of the experimentally determined single-Alexa647 or single-TMR intensity distribution pdf_{mono} was further used to calculate dimeric (pdf_{di}) and higher multimeric (pdf_{tri} and pdf_{quat}) intensity distributions based on iterative convolutions of pdf_{mono} as described previously (52). To reveal the stoichiometry of the protein complex, a linear combination of pdf_{mono}, pdf_{di}, pdf_{tri}, and pdf_{quat} was fitted to individual pdf_{RNP} distributions using a least squares method, taking into account the given protein and RNA labeling ratios.

SUPPLEMENTARY MATERIALS

Supplementary material for this article is available at <http://advances.sciencemag.org/cgi/content/full/6/11/eaaz1588/DC1>

Fig. S1. Assay schematic, coomassie gels of used proteins, tracking data and bleaching controls.

Fig. S2. Coomassie gels of used proteins, SEC-MALS data and minimal APC-fragment controls.

Fig. S3. Coomassie gel of the used protein and tracking data of immobilized motor proteins.

Table S1. Sequence of RNA fragments used.

Table S2. Labeling ratios (in percentage) of proteins and RNAs used in this study.

Movie S1. The kinesin-2 KIF3A/B/KAP3 and APC transport an axonal mRNA.

Movie S2. Cotransport of APC- β 2B-tubulin RNA complexes.

Movie S3. APC binds and diffuses on the microtubule lattice in the absence of kinesin-2.

Movie S4. APC- β 2B-tubulin RNA complexes diffuse on the microtubule lattice.

Movie S5. APC recruits and activates the heterotrimeric kinesin-2 KIF3A/B/KAP3.

Movie S6. Single-particle tracking of transported β 2B-tubulin RNA.

Movie S7. Quadruple-color movie illustrating the selectivity of the reconstituted mRNA transport system.

Movie S8. The APC-KIF3A/B/KAP3 mRNA transport system selectively transports β -actin RNA.

Movie S9. β -actin and β 2B-tubulin RNAs are transported in individual packages by the APC-KIF3A/B/KAP3 complex.

REFERENCES AND NOTES

1. A. R. Buxbaum, G. Haimovich, R. H. Singer, In the right place at the right time: Visualizing and understanding mRNA localization. *Nat. Rev. Mol. Cell Biol.* **16**, 95–109 (2015).
2. R. J. Weatheritt, T. J. Gibson, M. M. Babu, Asymmetric mRNA localization contributes to fidelity and sensitivity of spatially localized systems. *Nat. Struct. Mol. Biol.* **21**, 833–839 (2014).
3. C. E. Holt, S. L. Bullock, Subcellular mRNA localization in animal cells and why it matters. *Science* **326**, 1212–1216 (2009).
4. G. Tushev, C. Glock, M. Heumüller, A. Biever, M. Jovanovic, E. M. Schuman, Alternative 3' UTRs modify the localization, regulatory potential, stability, and plasticity of mRNAs in neuronal compartments. *Neuron* **98**, 495–511.e496 (2018).
5. J. M. Taliaferro, M. Vidaki, R. Oliveira, S. Olson, L. Zhan, T. Saxena, E. T. Wang, B. R. Graveley, F. B. Gertler, M. S. Swanson, C. B. Burge, Distal alternative last exons localize mRNAs to neural projections. *Mol. Cell* **61**, 821–833 (2016).
6. S. Mili, K. Moissoglu, I. G. Macara, Genome-wide screen reveals APC-associated RNAs enriched in cell protrusions. *Nature* **453**, 115–119 (2008).
7. A. E. Moor, M. Golan, E. E. Massasa, D. Lemze, T. Weizman, R. Shenhav, S. Baydatch, O. Mizrahi, R. Winkler, O. Golani, N. Stern-Ginossar, S. Itzkovitz, Global mRNA polarization regulates translation efficiency in the intestinal epithelium. *Science* **357**, 1299–1303 (2017).
8. S. Baumann, J. König, J. Koepke, M. Feldbrügge, Endosomal transport of septin mRNA and protein indicates local translation on endosomes and is required for correct septin filamentation. *EMBO Rep.* **15**, 94–102 (2014).

9. K. C. Martin, A. Ephrussi, mRNA localization: Gene expression in the spatial dimension. *Cell* **136**, 719–730 (2009).
10. H. Y. Park, H. Lim, Y. J. Yoon, A. Follenzi, C. Nwokafor, M. Lopez-Jones, X. Meng, R. H. Singer, Visualization of dynamics of single endogenous mRNA labeled in live mouse. *Science* **343**, 422–424 (2014).
11. B. Turner-Bridger, M. Jakobs, L. Muresan, H. H.-W. Wong, K. Franze, W. A. Harris, C. E. Holt, Single-molecule analysis of endogenous β -actin mRNA trafficking reveals a mechanism for compartmentalized mRNA localization in axons. *Proc. Natl. Acad. Sci. U.S.A.* **115**, E9697–E9706 (2018).
12. R. Fritzsche, D. Karra, K. L. Bennett, F. Ang, J. E. Heraud-Farlow, M. Tolino, M. Doyle, K. E. Bauer, S. Thomas, M. Planayavsky, E. Arn, A. Bakosova, K. Jungwirth, A. Hörmann, Z. Palfi, J. Sandholzer, M. Schwarz, P. Macchi, J. Colinge, G. Superti-Furga, M. A. Kiebler, Interactome of two diverse RNA granules links mRNA localization to translational repression in neurons. *Cell Rep.* **5**, 1749–1762 (2013).
13. Y. Kanai, N. Dohmae, N. Hirokawa, Kinesin transports RNA: Isolation and characterization of an RNA-transporting granule. *Neuron* **43**, 513–525 (2004).
14. M. A. McClintock, C. I. Dix, C. M. Johnson, S. H. McLaughlin, R. J. Maizels, H. T. Hoang, S. L. Bullock, RNA-directed activation of cytoplasmic dynein-1 in reconstituted transport RNP. *eLife* **7**, e36312 (2018).
15. T. E. Sladewski, C. S. Bookwalter, M.-S. Hong, K. M. Trybus, Single-molecule reconstitution of mRNA transport by a class V myosin. *Nat. Struct. Mol. Biol.* **20**, 952–957 (2013).
16. F. T. Edelmann, A. Schlundt, R. G. Heym, A. Jenner, A. Niedner-Boblentz, M. I. Syed, J.-C. Paillart, R. Stehle, R. Janowski, M. Sattler, R.-P. Jansen, D. Niessing, Molecular architecture and dynamics of *ASH1* mRNA recognition by its mRNA-transport complex. *Nat. Struct. Mol. Biol.* **24**, 152–161 (2017).
17. T. E. Sladewski, N. Billington, M. Y. Ali, C. S. Bookwalter, H. Lu, E. B. Kremntsova, T. A. Schroer, K. M. Trybus, Recruitment of two dyneins to an mRNA-dependent Bicaudal D transport complex. *eLife* **7**, e36306 (2018).
18. T. Jimbo, Y. Kawasaki, R. Koyama, R. Sato, S. Takada, K. Haraguchi, T. Akiyama, Identification of a link between the tumour suppressor APC and the kinesin superfamily. *Nat. Cell Biol.* **4**, 323–327 (2002).
19. S. Munemitsu, B. Souza, O. Müller, I. Albert, B. Rubinfeld, P. Polakis, The APC gene product associates with microtubules in vivo and promotes their assembly in vitro. *Cancer Res.* **54**, 3676–3681 (1994).
20. J. Zumbunn, K. Kinoshita, A. A. Hyman, I. S. Näthke, Binding of the adenomatous polyposis coli protein to microtubules increases microtubule stability and is regulated by GSK3 β phosphorylation. *Curr. Biol.* **11**, 44–49 (2001).
21. N. Preitner, J. Quan, D. W. Nowakowski, M. L. Hancock, J. Shi, J. Tcherkezian, T. L. Young-Pearse, J. G. Flanagan, APC is an RNA-binding protein, and its interactome provides a link to neural development and microtubule assembly. *Cell* **158**, 368–382 (2014).
22. P. T. Ruane, L. F. Gumy, B. Bola, B. Anderson, M. J. Wozniak, C. C. Hoogenraad, V. J. Allan, Tumour suppressor adenomatous polyposis coli (APC) localisation is regulated by both Kinesin-1 and Kinesin-2. *Sci. Rep.* **6**, 27456 (2016).
23. J. Scholz, H. Besir, C. Strasser, S. Suppmann, A new method to customize protein expression vectors for fast, efficient and background free parallel cloning. *BMC Biotechnol.* **13**, 12 (2013).
24. F. Weissmann, G. Petzold, R. VanderLinden, P. J. Huis in 't Veld, N. G. Brown, F. Lampert, S. Westermann, H. Stark, B. A. Schulman, J.-M. Peters, biGbac enables rapid gene assembly for the expression of large multisubunit protein complexes. *Proc. Natl. Acad. Sci. U.S.A.* **113**, E2564–E2569 (2016).
25. A. Keppler, S. Gendreizig, T. Gronemeyer, H. Pick, H. Vogel, K. Johnsson, A general method for the covalent labeling of fusion proteins with small molecules in vivo. *Nat. Biotechnol.* **21**, 86–89 (2003).
26. D. A. Zacharias, J. D. Violin, A. C. Newton, R. Y. Tsien, Partitioning of lipid-modified monomeric GFPs into membrane microdomains of live cells. *Science* **296**, 913–916 (2002).
27. J.-Y. Tinevez, N. Perry, J. Schindelin, G. M. Hoopes, G. D. Reynolds, E. Laplantine, S. Y. Bednarek, S. L. Shorte, K. W. Eliceiri, TrackMate: An open and extensible platform for single-particle tracking. *Methods* **115**, 80–90 (2017).
28. N. Tarantino, J.-Y. Tinevez, E. F. Crowell, B. Boisson, R. Henriques, M. Mhlanga, F. Agou, A. Israël, E. Laplantine, TNF and IL-1 exhibit distinct ubiquitin requirements for inducing NEMO-IKK supramolecular structures. *J. Cell Biol.* **204**, 231–245 (2014).
29. S. Takeda, H. Yamazaki, D.-H. Seog, Y. Kanai, S. Terada, N. Hirokawa, Kinesin superfamily protein 3 (KIF3) motor transports fodrin-associating vesicles important for neurite building. *J. Cell Biol.* **148**, 1255–1265 (2000).
30. J. O. L. Andreasson, S. Shastry, W. O. Hancock, S. M. Block, The mechanochemical cycle of mammalian kinesin-2 KIF3A/B under load. *Curr. Biol.* **25**, 1166–1175 (2015).
31. J.-M. Cioni, J. Q. Lin, A. V. Holtermann, M. Koppers, M. A. H. Jakobs, A. Azizi, B. Turner-Bridger, T. Shigeoka, K. Franze, W. A. Harris, C. E. Holt, Late endosomes act as mRNA translation platforms and sustain mitochondria in axons. *Cell* **176**, 56–72.e15 (2019).
32. J. S. Liu, C. R. Schubert, X. Fu, F. J. Fourmiol, J. K. Jaiswal, A. Houdusse, C. M. Stultz, C. A. Moores, C. A. Walsh, Molecular basis for specific regulation of neuronal kinesin-3 motors by doublecortin family proteins. *Mol. Cell* **47**, 707–721 (2012).
33. B. Y. Monroy, D. L. Sawyer, B. E. Ackermann, M. M. Borden, T. C. Tan, K. M. Ori-McKenney, Competition between microtubule-associated proteins directs motor transport. *Nat. Commun.* **9**, 1487 (2018).
34. P. J. Hooikaas, M. Martin, T. Mühlethaler, G.-J. Kuijntjes, C. A. E. Peeters, E. A. Katrukha, L. Ferrari, R. Stucchi, D. G. F. Verhagen, W. E. van Riel, I. Grigoriev, A. F. M. Altaear, C. C. Hoogenraad, S. G. D. Rüdiger, M. O. Steinmetz, L. C. Kapitein, A. Akhmanova, MAP7 family proteins regulate kinesin-1 recruitment and activation. *J. Cell Biol.* **218**, 1298–1318 (2019).
35. J. Deka, J. Kuhlmann, O. Müller, A domain within the tumor suppressor protein APC shows very similar biochemical properties as the microtubule-associated protein tau. *Eur. J. Biochem.* **253**, 591–597 (1998).
36. Z. Li, K. Kroboth, I. P. Newton, I. S. Näthke, Novel self-association of the APC molecule affects APC clusters and cell migration. *J. Cell Sci.* **121**, 1916–1925 (2008).
37. Z. Li, I. S. Näthke, Tumor-associated NH₂-terminal fragments are the most stable part of the adenomatous polyposis coli protein and can be regulated by interactions with COOH-terminal domains. *Cancer Res.* **65**, 5195–5204 (2005).
38. M. Batish, P. van den Bogaard, F. R. Kramer, S. Tyagi, Neuronal mRNAs travel singly into dendrites. *Proc. Natl. Acad. Sci. U.S.A.* **109**, 4645–4650 (2012).
39. M. Mikl, G. Vendra, M. A. Kiebler, Independent localization of *MAP2*, *CaMKII α* and β -actin RNAs in low copy numbers. *EMBO Rep.* **12**, 1077–1084 (2011).
40. L. J. Carithers, K. Ardlie, M. Barcus, P. A. Branton, A. Britton, S. A. Buia, C. C. Compton, D. S. DeLuca, J. Peter-Demchok, E. T. Gelfand, P. Guan, G. E. Korzeniewski, N. C. Lockhart, C. A. Rabiner, A. K. Rao, K. L. Robinson, N. V. Roche, S. J. Sawyer, A. V. Segre, C. E. Shive, A. M. Smith, L. H. Sobin, A. H. Undale, K. M. Valentino, J. Vaught, T. R. Young, H. M. Moore; GTEx Consortium, A novel approach to high-quality postmortem tissue procurement: The GTEx project. *Biopreserv. Biobank.* **13**, 311–319 (2015).
41. Y. J. Yoon, B. Wu, A. R. Buxbaum, S. Das, A. Tsai, B. P. English, J. B. Grimm, L. D. Lavis, R. H. Singer, Glutamate-induced RNA localization in neurons. *Proc. Natl. Acad. Sci. U.S.A.* **113**, E6877–E6886 (2016).
42. J. R. Cooper, L. Wordeman, The diffusive interaction of microtubule binding proteins. *Curr. Opin. Cell Biol.* **21**, 68–73 (2009).
43. M. S. Song, H. C. Moon, J.-H. Jeon, H. Y. Park, Neuronal messenger ribonucleoprotein transport follows an aging levy walk. *Nat. Commun.* **9**, 344 (2018).
44. T. J. Messitt, J. A. Gagnon, J. A. Kreiling, C. A. Pratt, Y. J. Yoon, K. L. Mowry, Multiple kinesin motors coordinate cytoplasmic RNA transport on a subpopulation of microtubules in *Xenopus* oocytes. *Dev. Cell* **15**, 426–436 (2008).
45. J. B. Dichtenberg, S. A. Swanger, L. N. Antar, R. H. Singer, G. J. Bassell, A direct role for FMRP in activity-dependent dendritic mRNA transport links filopodial-spine morphogenesis to fragile X syndrome. *Dev. Cell* **14**, 926–939 (2008).
46. M. Nakamura, X. Z. Zhou, K. P. Lu, Critical role for the EB1 and APC interaction in the regulation of microtubule polymerization. *Curr. Biol.* **11**, 1062–1067 (2001).
47. D. Breitsprecher, R. Jaiswal, J. P. Bombardier, C. J. Gould, J. Gelles, B. L. Goode, Rocket launcher mechanism of collaborative actin assembly defined by single-molecule imaging. *Science* **336**, 1164–1168 (2012).
48. J. L. Henty-Ridilla, A. Rankova, J. A. Eskin, K. Kenny, B. L. Goode, Accelerated actin filament polymerization from microtubule plus ends. *Science* **352**, 1004–1009 (2016).
49. S. A. I. Seidel, P. M. Dijkman, W. A. Lea, G. van den Bogaard, M. Jerabek-Willemsen, A. Lazić, J. S. Joseph, P. Srinivasan, P. Baas, A. Simeonov, I. Katritch, F. A. Melo, J. E. Ladbury, G. Schreiber, A. Watts, D. Braun, S. Dühr, Microscale thermophoresis quantifies biomolecular interactions under previously challenging conditions. *Methods* **59**, 301–315 (2013).
50. P. Bieling, I. A. Telley, C. Henrich, J. Piehler, T. Surrey, in *Methods in Cell Biology* (Elsevier, ed. 1, 2010; [http://dx.doi.org/10.1016/S0091-679X\(10\)95028-0](http://dx.doi.org/10.1016/S0091-679X(10)95028-0)), vol. 95, pp. 555–580.
51. J. Schindelin, I. Arganda-Carreras, E. Frise, V. Kaynig, M. Longair, T. Pietzsch, S. Preibisch, C. Rueden, S. Saalfeld, B. Schmid, J.-Y. Tinevez, D. J. White, V. Hartenstein, K. Eliceiri, P. Tomancak, A. Cardona, Fiji: An open-source platform for biological-image analysis. *Nat. Methods* **9**, 676–682 (2012).
52. M. Moertelmaier, M. Brameshuber, M. Linmeier, G. J. Schütz, H. Stockinger, Thinning out clusters while conserving stoichiometry of labeling. *Appl. Phys. Lett.* **87**, 263903 (2005).

Acknowledgments: We thank the CRG BMS-PT core facility for support by providing reagents and training on instrumentation. We further thank T. Surrey, V. Malhotra, I. Telley, C. Duellberg, and M. Feldbruegge for critical comments on the manuscript. **Funding:** This work was funded by the Spanish Ministry of Economy and Competitiveness (MINECO) (BFU2017-85361-P, BFU2014-54278-P, and BFU2015-62550-ERC), Juan de la Cierva-Incorporación Program (IJC1-2015-25994), the Human Frontiers in Science Program (HFSP) (RGY0083/2016), and the European Research Council (ERC) (H2020-MSCA-IF-2014-659271). V.R. acknowledges support from the Spanish Ministry of Economy and Competitiveness through the Program “Centro de Excelencia Severo Ochoa 2013–2017,” the CERCA Programme/Generalitat de

Catalunya, MINECO's Plan Nacional (BFU2017-86296-P). S.W. acknowledges support from the Spanish Ministry of Economy and Competitiveness through the "Severo Ochoa" program for Centres of Excellence in R&D (SEV-2015-0522), from Fundació Privada Cellex, and from Generalitat de Catalunya through the CERCA program. We further acknowledge support of the Spanish Ministry of Economy and Competitiveness (MEIC) to the EMBL partnership, "Centro de Excelencia Severo Ochoa" (SEV-2012-0208) and the CERCA Programme/Generalitat de Catalunya. **Author contributions:** S.B. and S.P.M. conceived the project. S.B., M.G., A.K., and S.P.M. performed the experiments. S.B., V.R., S.W., and S.P.M. analyzed the data. S.B. and S.P.M. wrote the article. S.P.M. supervised the project. **Competing interests:** The authors declare that they have no competing interests. **Data and materials availability:** All data needed to evaluate the conclusions in the paper are present in the paper

and/or the Supplementary Materials. Additional data related to this paper may be requested from the authors.

Submitted 16 August 2019
Accepted 17 December 2019
Published 13 March 2020
10.1126/sciadv.aaz1588

Citation: S. Baumann, A. Komissarov, M. Gili, V. Ruprecht, S. Wieser, S. P. Maurer, A reconstituted mammalian APC-kinesin complex selectively transports defined packages of axonal mRNAs. *Sci. Adv.* **6**, eaaz1588 (2020).